Supplementary Information

Dual Stimuli-Responsive Smart Soft Carrier Using Multi-material 4D Printing

Inyoung Choi[a,#], Saeeun Jang[b,#], Seunggyeom Jung[a,#], Seohyun Woo[a], Jinyoung Kim[a], Cheol Bak[c], Yongmin Lee[c,d] and Sukho Park[a,b,*]

[a]School of Undergraduate Studies, Daegu Gyeongbuk Institute of Science & Technology (DGIST), Daegu 42988 South Korea.
[b]Department of Robotics and Mechatronics Engineering, Daegu Gyeongbuk Institute of Science & Technology (DGIST), Daegu 42988 South Korea.
[c]Department of Energy Science and Engineering, Daegu Gyeongbuk Institute of Science & Technology (DGIST), Daegu 42988 South Korea.
[d]Energy Science and Engineering Center, Daegu Gyeongbuk Institute of Science & Technology (DGIST), Daegu 42988 South Korea

#These authors contributed equally to this work
 * Corresponding author. E-mail: shpark12@dgist.ac.kr

Supplementary Materials and Methods

Materials

N-Isopropylacrylamide≥99% (NIPAM), N, N-methylenebisacrylamide≥99.5% (BIS), poly (ethylene glycol) diacrylate, average Mn 700 (PEGDA), Pluronic F-127 (PF127), and magnetic iron oxide nanoparticles(MNPs) were purchased from Sigma-Aldrich. 2,2-diethoxyacetophenone was purchased from the Tokyo chemical industry. A planetary centrifugal mixer (ARM-310, Thinky) was used to mix materials. Near-infrared (NIR) laser (FL-DLS21-000003, Focuslight)

Fabrication of biocompatible citric acid-coated SPIONs

SPIONs coated with citric acid were manufactured using the co-precipitation method. To prevent oxidation of the SPIONs during the manufacturing process, the inlets of the three-necked flask were sealed with stoppers to prevent O_2 from entering, and N_2 purging was continuously performed. First, 22.60 wt% iron (III) chloride ($FeCl_3$) (14.6 g) and 19.35 wt% iron (II) chloride tetrahydrate ($FeCl_2 \cdot 4H_2O$) (12 g) were dissolved in DI water (50 ml),[1] and the temperature was increased to 80 °C with magnetic stirring at 400 rpm to mix the solution uniformly. When the temperature of the mixed solution reached 80 °C, ammonia water (200 ml) was dropped over 1.5 h using a dropping funnel, and the mixture was magnetically stirred for 1 h to precipitate the SPIONs. Subsequently, a mixture of 10.71 wt% citric acid (6 g) in DI water (50 ml) was added and magnetic stirring continued for an additional 1 h such that the citric acid was well coated on the SPIONs.[2] When the reaction process was complete, the mixture was cooled down to 25 °C. The washing process was repeated several times using DI water (200 ml), and the supernatant liquid containing excess citric acid and other impurities was removed using magnetic separation. After the washing process, the collected citric acid-coated SPIONs were homogeneously dispersed in DI water (150 ml), freeze-dried, and ground in a mortar to prevent clumping.

Preparation of printing inks

PNIPAM, PEG, and PEG with SPIONs inks used for 4D printing were prepared through the following processes.[3] To make PNIPAM and PEG inks, hydrogel precursor solution, fugitive carrier (PF127) 24.7 wt% (5 g), and a photo-initiator (2,2-diethoxy acetophenone) 1.8 wt%(386 μL) were added to deionized water (DW) 61.2 wt% (12.4 ml), where the PNIPAM precursor solution was NIPAM 9.9 wt% (2 g) with the crosslinking agent BIS 2.5 wt% (500 mg), and the PEG precursor solution was PEGDA 11.14 wt% (1964 μL). Each mixture was mixed using a mixer at 2000 rpm for 6 minutes. Finally, PNIPAM and PEG inks were purged with nitrogen to remove air bubbles and stored at 4 °C overnight. To make PEG with SPIONs ink, 5 wt% of SPIONs (1.1 g) was added to the PEG ink and mixed with a mixer at 2000 rpm for 150 s. After sonication for 30 s to uniformly disperse the SPIONs in the PEG ink, the mixture was placed at -18 °C for 15 minutes to be liquified. The produced PNIPAM, PEG, and PEG with SPIONs inks were transferred to a 12 ml Luer-lock type syringe, respectively, and stored for 2 h at room temperature to gain appropriate viscosity for 3D printing before use.

Rheological Measurements of hydrogel inks

The rheological measurements of the hydrogel inks were measured using a rheometer (MCR92, Anton Paar) with a 25 mm diameter plate and 1mm gap at 25 °C. Shear strain sweep tests were performed, 1 Hz over the strain range of 0.1–1000 %. Viscosity tests were performed in the shear rate range of 0.1–100 s^{-1}.

3D printing apparatus and protocol
After modeling the 3D structure using the SketchUp program (Trimble, Inc.), the 3D structure model for 3D printing was extracted as a stereolithography (STL) file and converted to a GCODE file. The 3D structure was printed using a direct ink writing (DIW)-based ROKIT INVIVO Bio 3D printer (ROKIT Healthcare, Inc.). The 3D printing set parameters are described in Supplementary Figure S1. The lid part (PNIPAM ink), border part (PEG with SPIONs ink), and hemisphere part (PEG ink) of the robot were printed using syringes with diameters of 25G, 23G, and 25G needles, respectively. The syringe containing the ink to be printed was installed on the syringe dispenser of the 3D printer and leveled such that the distance between the needle of the syringe and the Petri dish was 200μm. A UV irradiator (365 nm) (Panasonic, UJ35) was used for the polymerization of the 3D-printed structure.
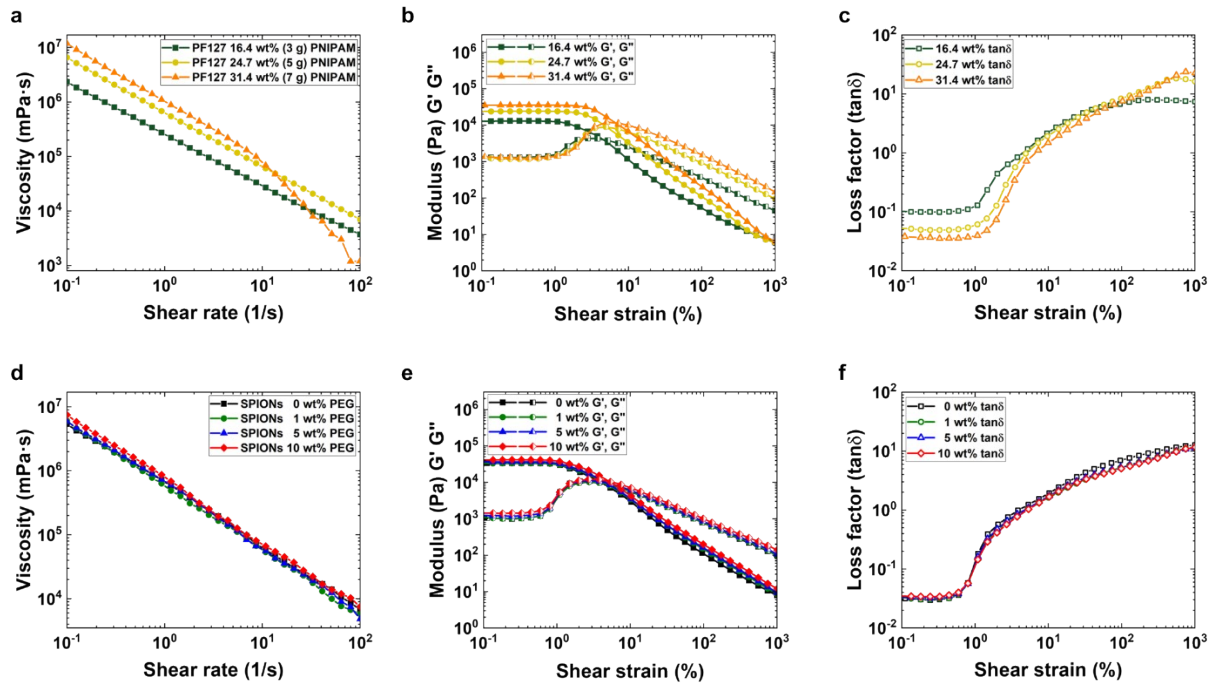
Supplementary Results

Figure S1. Rheological properties of PNIPAM inks according to PF127 concentration log-log plots of a) viscosity according to shear rate, b) storage and loss modulus according to shear strain, and c) loss factor according to shear strain. Rheological properties of PEG inks according to SPIONs concentration log-log plots of d) viscosity according to shear rate, e) storage and loss modulus according to shear strain, and f) loss factor according to shear strain.
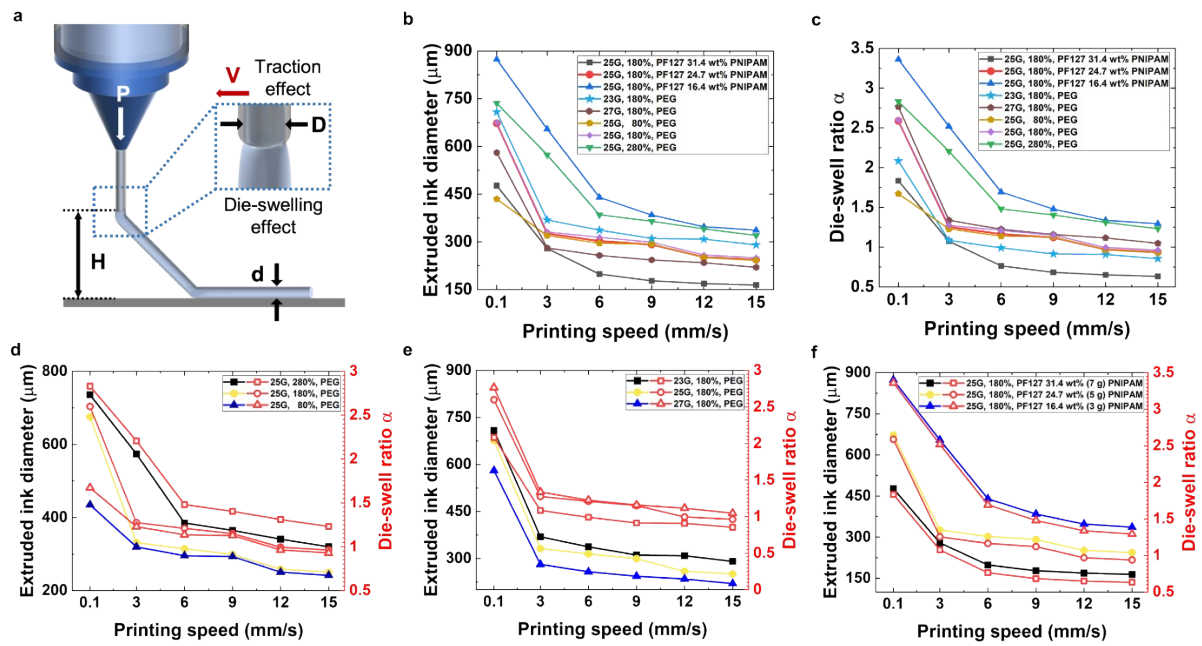
Figure S2. Die-swelling and traction effects and die-swell ratio of multi-materials. a) The schematic of die-swelling and traction effect. b) Extruded ink diameter and c) die-swell ratio according to printing speed for all conditions. Extruded ink diameter and die-swell ratio according to printing speed by d) extrusion amount, e) needle gauge, and f) PF127 concentration.
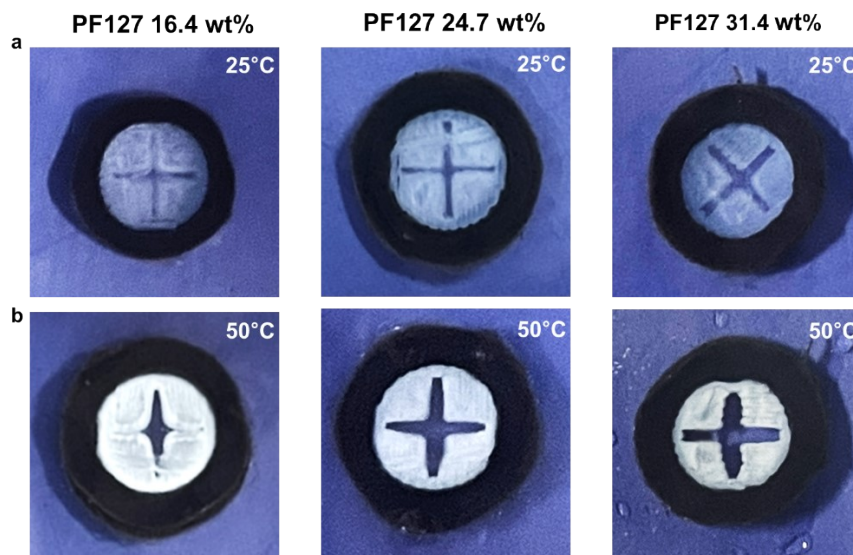

Figure S3. a) The image of the swelled lid composed of PNIPAM ink with 16.4wt% of PF127, 24.7wt% of PF127, and 31.4wt% of PF127 at 25 °C and b) shrunk lid composed of PNIPAM ink with 16.4wt% of PF127, 24.7wt% of PF127 and 31.4wt% of at 50 °C.
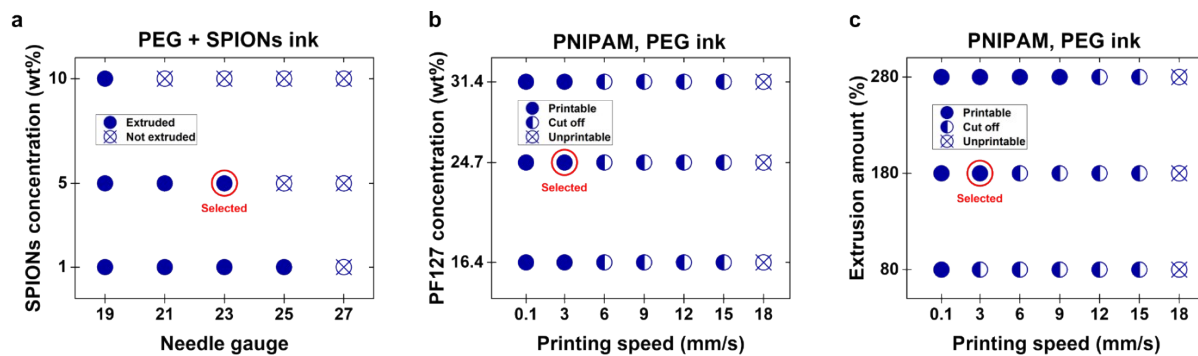
Figure S4. Printability tests of each ink. a) Printability of PEG with different concentrations of SPIONs ink according to needle gauge. Printability of PNIPAM, PEG ink according to printing speed by b) PF127 concentration and c) extrusion amount.
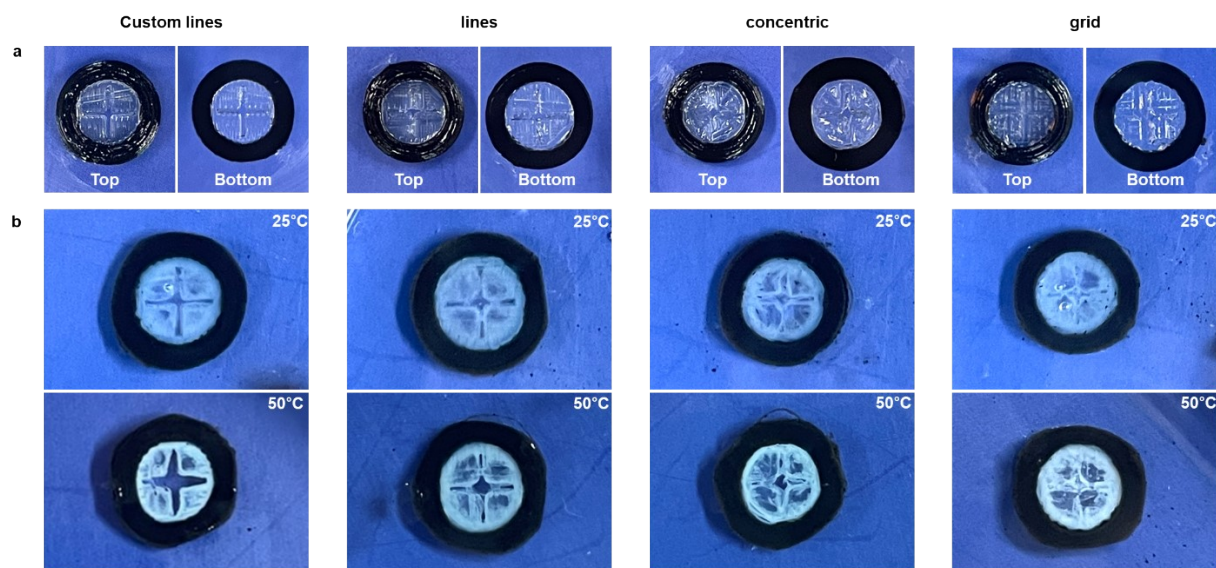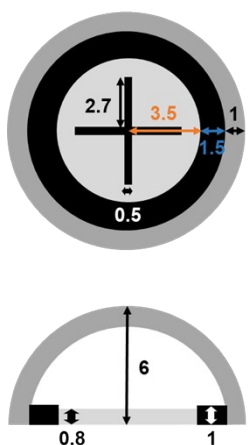

Figure S5. Printing quality and swelling/shrinking behavior according to printing path. a) Top and bottom view lid images by custom lines, lines, concentric, and grid after UV curing. b) The image of the swelled lid at 25 °C and the shrunk lid at 50 °C by custom lines, lines, concentric, and grid.

Parameter (General)		Parameter (Quality)	
Nozzle size (mm)	0.3	Height of first layer (mm)	0.2
Height of layer (mm)	0.2	Width ratio of line (%)	100
Density (%)	100	Retraction distance (mm)	0.5
Infill pattern	Custom lines	Loading before output (mm)	0.0
Rotation angle of infill (°)	90		
Angle of first layer infill (°)	180	Parameter (Skirt)	

Parameter (Skirt)	
Number of skirt line	1
Starting point (mm)	6
Minimum length (mm)	5

Parameter (Speed)	
Printing speed (mm/s)	3
Movement rate (mm/s)	3
Floor layer speed (mm/s)	3

Parameter (Filament)	
Extrusion amount (%)	180

Figure S6. 3D printer parameters setting

Structure (Ink) Type	Parameter	Modeling Value [mm]	Measure Value [mm]	Error [mm]
Lid (PNIPAM)	Diameter	7.0	6.35	0.65
	Height	0.8	0.79	0.01
	Slot Length	5.4	5.2	0.2
	Slot Width	0.5	0.56	0.06
Border (PEG+SPIONs)	Diameter	10	10.13	0.13
	Height	1	1.21	0.21
Hemisphere (PEG)	Diameter	12	11.87	0.13
	Height	6	5.96	0.04

Figure S7. Design model and summary of the error between the modeling and measured values of the actual 4D printed smart soft carrier.
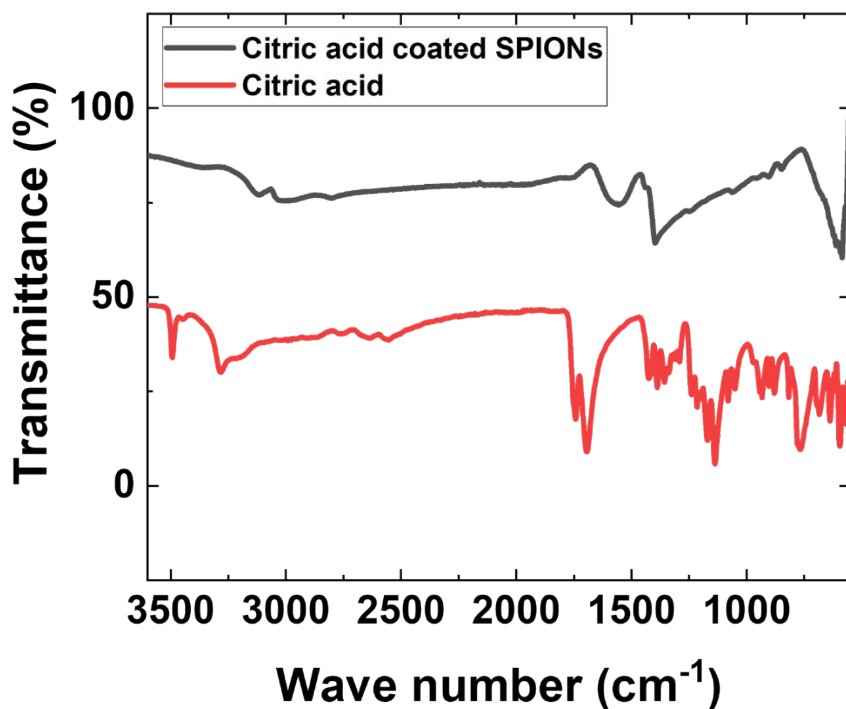
Figure S8. FT-IR spectra of citric acid and citric acid-coated SPIONs.
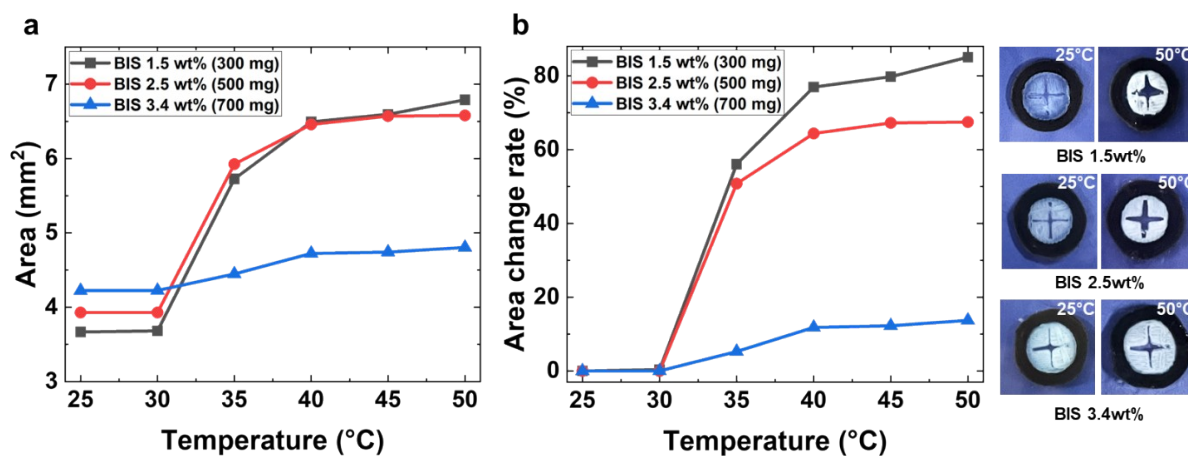

Figure S9. a) Slot area and b) slot area change rate according to the temperature of the lid-only construct with various concentrations of BIS. The image of the swelled and shrunk lid at 25 °C and 50 °C.
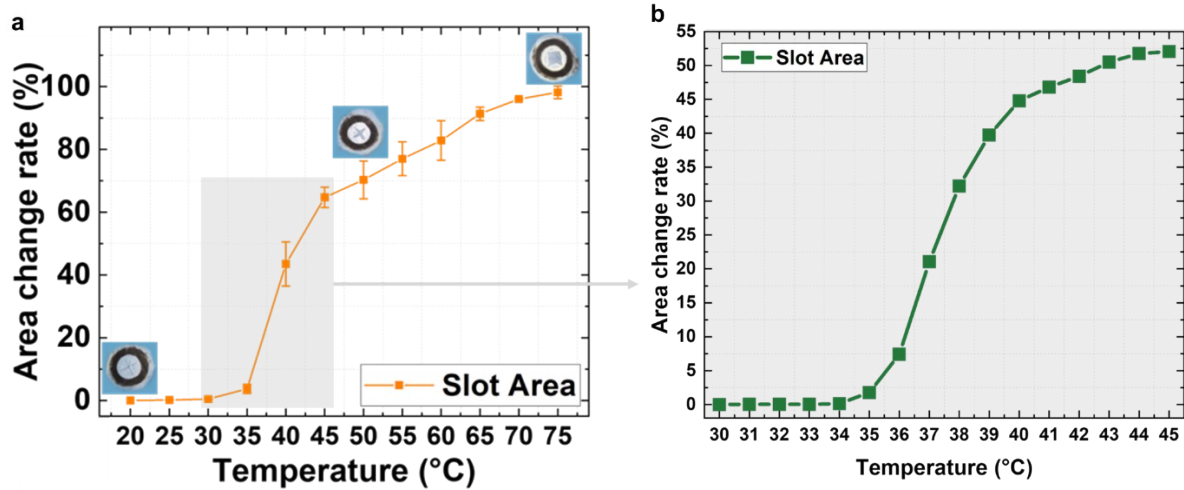
Figure S10. a) Slot area change rate of the smart soft carrier at 5 °C intervals when the temperature of the water is increased using a hot plate. b) LCST analysis graph through slot area change rate according to temperature.
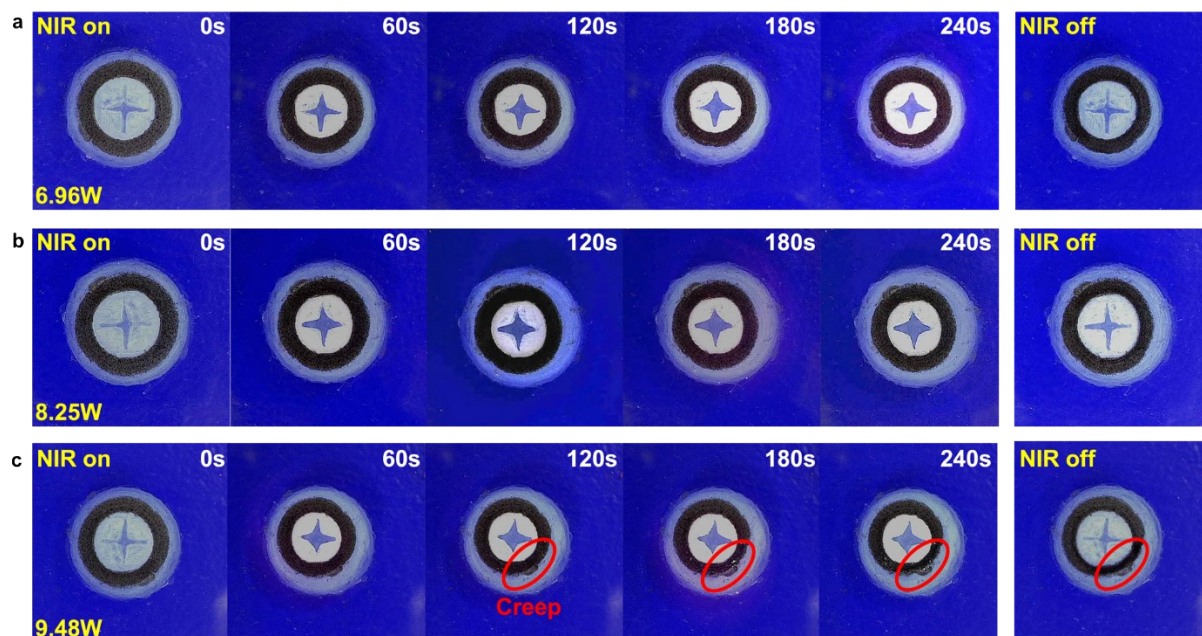
Figure S11. Examination of smart soft carrier creep during a 240 seconds irradiation of NIR intensity variations.
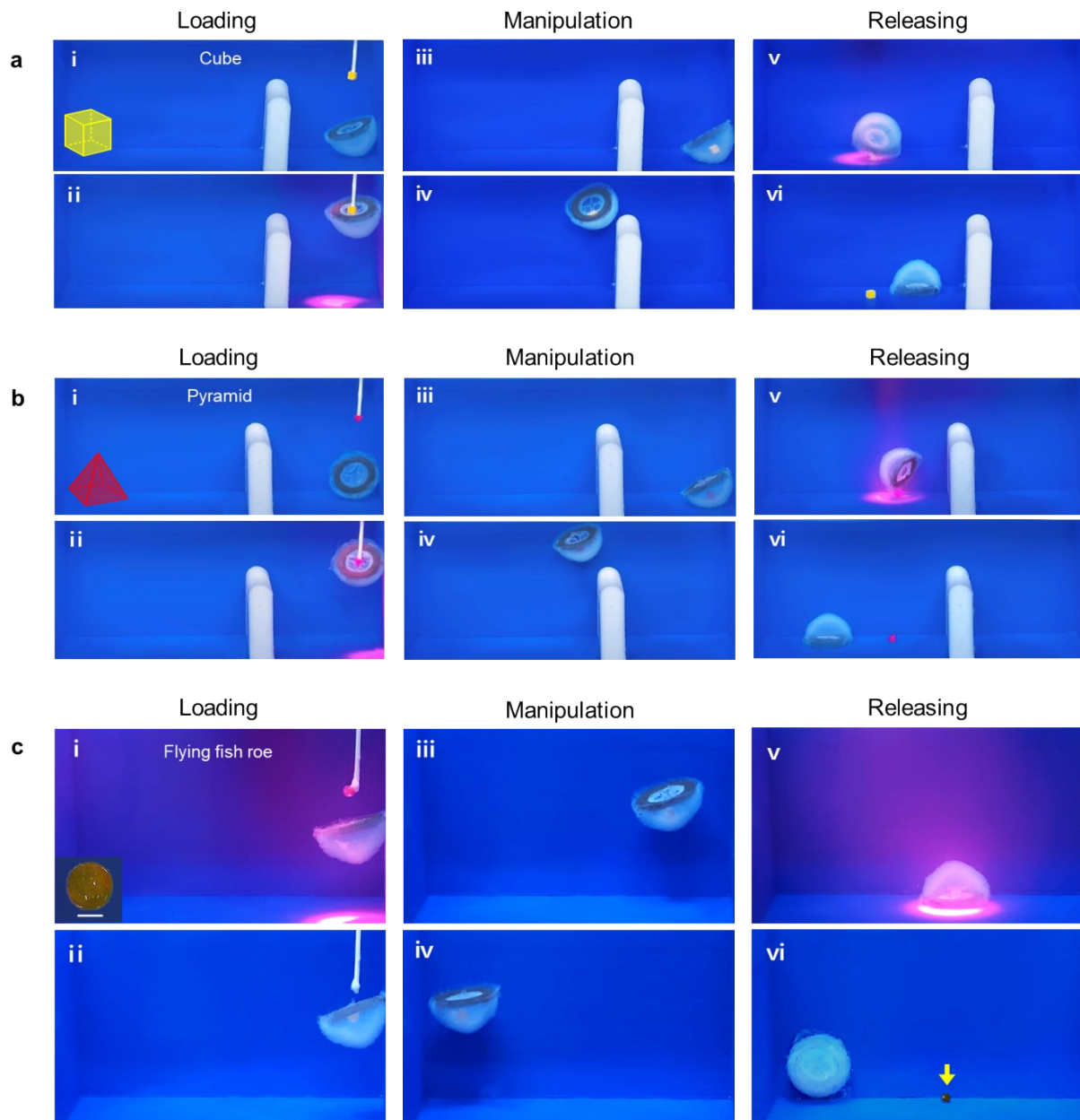
Figure S12. Delivery test of the smart soft carrier with cargo of various shapes and properties. a) Cube-shaped cargo delivery test. (i) Initial position of the smart soft carrier. (ii) Irradiate the NIR to open the slot and load the cube-shaped cargo. (iii) The cube-shaped cargo is safely loaded in the hemisphere part. (iv) It jumps over an obstacle with cargo loaded. (v) The slot is opened, and the cargo exits the smart soft carrier due to convection. (vi) The slot closes after the NIR irradiation is stopped, and the smart soft carrier is placed next to the exited cargo. b) Pyramid-shaped cargo delivery test. (i) Initial position of the smart soft carrier under the pyramid-shaped cargo attached to the rod. (ii) Pyramid-shaped cargo is loaded through the opened slot. (iii) It is checked whether the pyramid-shaped cargo is loaded in the hemisphere part. (iv) Overcome an obstacle while safely loading the pyramid-shaped cargo. (v) NIR irradiation is started to open the slot and check that the pyramid-shaped cargo has exited the smart soft carrier due to convection. (vi) The smart soft carrier is positioned next to the cargo that escaped, and the NIR irradiation is stopped to close the slot. c) Flying fish roe delivery test. (i) After moving the smart soft carrier up the z-axis to the position where a flying fish roe is placed, the slot is

opened by irradiating NIR. Scale bar: 0.1 cm (ii) After the slot is closed by removing the NIR, the flying fish roe is loaded into the smart soft carrier due to the closing of the slot. The (iii) z-axis movement and (iv) x-axis movement are checked using an external magnetic field. (v) Irradiate the NIR to open the slot. (vi) The flying fish roe is released from the smart soft carrier.

Magnetic manipulation and Disturbance
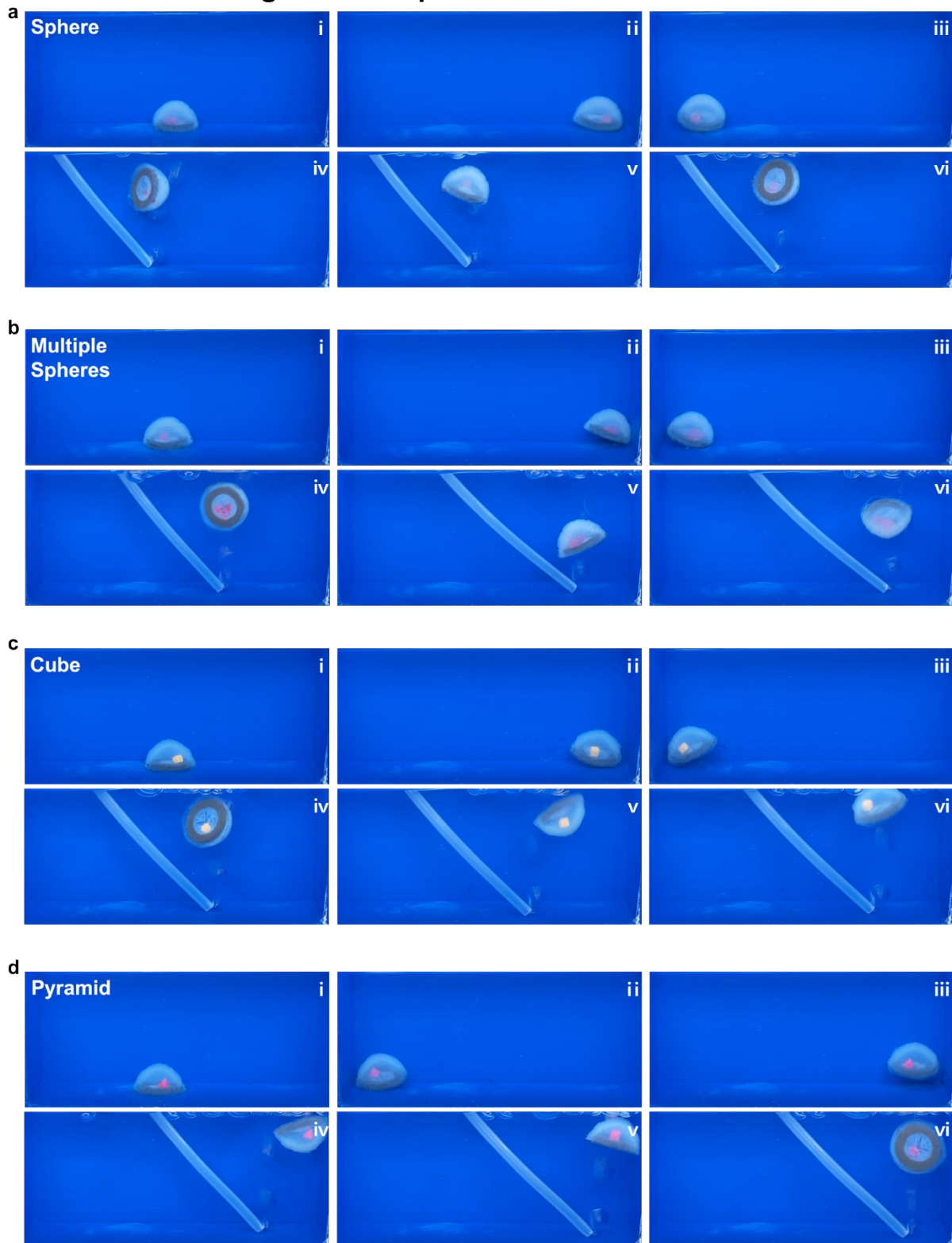
Figure S13. Magnetic manipulation and robustness test of the smart soft carrier on external disturbance. a) (i), (ii), (iii) Magnetic manipulation of the smart soft carrier contained sphere-shaped cargo was performed with the lid facing the floor. (iv), (v), (vi) The smart soft carrier was rotated 360° by air bubbles, the sphere-shaped cargo loaded inside was safely located in its inner space. b) (i), (ii), (iii) Magnetic manipulation of the smart soft

carrier contained multiple sphere-shaped cargoes was performed with the lid facing the floor. (iv), (v), (vi) The smart soft carrier was rotated 360° by air bubbles, the multiple sphere-shaped cargoes loaded inside was safely located in its inner space. c) (i), (ii), (iii) Magnetic manipulation of the smart soft carrier contained cube-shaped cargo was performed with the lid facing the floor. (iv), (v), (vi) The smart soft carrier was rotated 360° by air bubbles, the cube-shaped cargo loaded inside was safely located in its inner space. d) (i), (ii), (iii) Magnetic manipulation of the smart soft carrier contained pyramid-shaped cargo was performed with the lid facing the floor. (iv), (v), (vi) The smart soft carrier was rotated 360° by air bubbles, and the pyramid-shaped cargo loaded inside was safely located in its inner space.
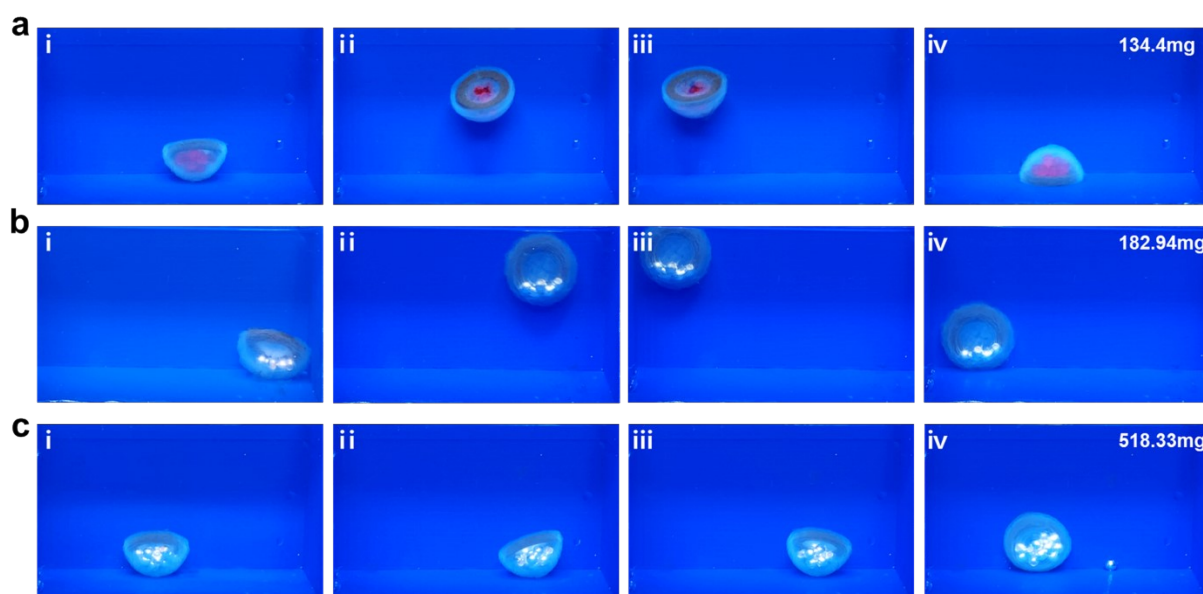
Figure S14. Cargo handling capability of the smart soft carrier by measuring the maximum number and mass of handling cargoes. a) (i) Smart soft carrier contained 12 polymer sphere-shaped cargoes. The cargo had a diameter of 2.6mm. The total weight of the cargoes was 134.4 mg. The smart soft carrier could be driven along the (ii) z-axis and (iii) x-axis while loading cargoes. (iv) There was no separation of the smart soft carrier structure, and no cargo escaped from the smart soft carrier. b) (i) Smart soft carrier contained 6 silver sphere-shaped cargoes. The cargo had a diameter of 2.5mm. The total weight of the cargoes was 182.94 mg. The smart soft carrier could be driven along the (ii) z-axis and (iii) x-axis while loading cargoes. (iv) There was no separation of the smart soft carrier structure, and no cargo escaped from the smart soft carrier. c) (i) Smart soft carrier contained 17 silver sphere-shaped cargoes. The cargo had a diameter of 2.5mm. The total weight of cargoes was 518.33 mg. (ii) The smart soft carrier could be not driven along the z-axis. (iii) The smart soft carrier could be driven along the x-axis. (iv) One cargo escaped out of the smart soft carrier.

Sea monkey
i — Trapping
ii — Disturbance
iii — Disturbance
iv — Releasing

Guppy baby
i — Trapping
ii — Disturbance
iii — Disturbance
iv — Releasing
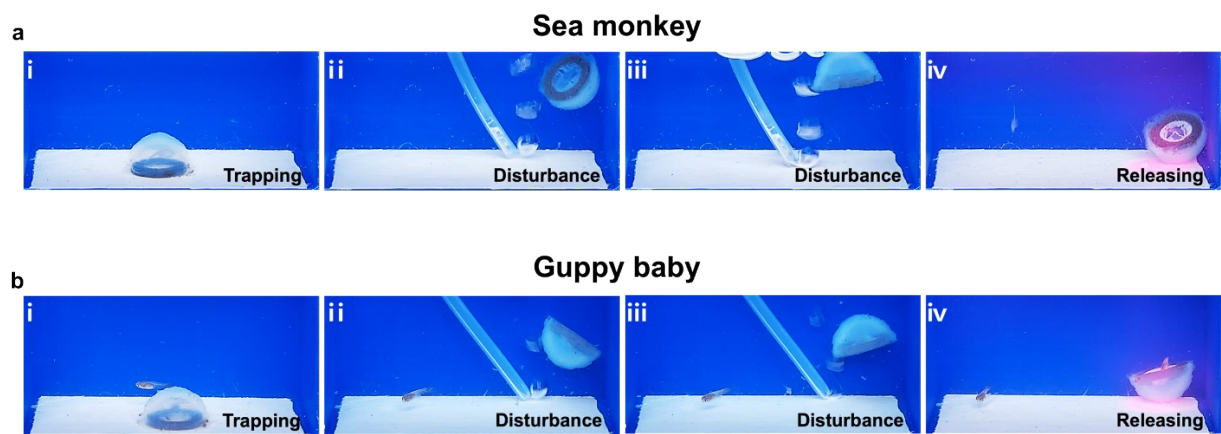
Figure S15. Robustness of the smart soft carrier with living marine organisms on external disturbance. a) (i) Sea monkey trapped inside the smart soft carrier. (ii) (iii) Sea monkey stably trapped despite strong rotation of the smart soft carrier owing to the air injection as an external disturbance. (iv) Trapped sea monkey released alive through the opened slot after NIR irradiation. b) (i) Guppy baby trapped inside the smart soft carrier. (ii) (iii) Guppy baby stably trapped despite strong rotation of the smart soft carrier owing to the air injection as an external disturbance. (iv) Trapped guppy baby released alive through the opened slot after NIR irradiation.

Hydrogel Actuator	Fabrication method	Multi-stimuli responsive	Untethered manipulation	Cargo delivery	Fragile Cargo delivery	Available cargo shape	Multiple cargoes	Handling of living organisms	Disturbance test
Our smart soft carrier	4D printing	○ (Magnetic field, thermo)	○	○	○	(Sphere, cube, pyramid)	○	○ (Sea monkey, Guppy baby)	○
Hydraulic hydrogel actuator[4]	Molding	× (Pneumatic)	×	×	×	×	×	○ (Goldfish)	×
Camouflageable hydrogel gripper[5]	4D printing	× (Humidity)	×	○	×	(Sphere)	×	○ (Goldfish)	×
Hybrid soft millirobot[6]	4D printing	○ (Magnetic field, thermos)	○	○	×	(Sphere)	×	○ (Cell)	○
Microgripper[7]	Photolithography	○ (Magnetic field, thermo)	○	○	×	(Sphere)	○	○ (Cell)	×
Untethered milli-gripper[8]	4D printing	○ (Magnetic field, electric field)	○	○	×	(Sphere, cube, frog, star)	○	×	×
Magnetic hydrogel wheel[9]	4D printing	× (Magnetic field)	○	○	×	(Tube)	×	×	×
Stimuli responsive gripper with hole[10]	Molding	○ (pH, thermo)	○	○	×	(Star, triangular pillar, cube, tube)	×	×	○
Hybrid hydrogel gripper[11]	4D printing	○ (Magnetic field, thermo)	○	○	○	(Sphere)	×	×	×
Four-armed gel gripper[12]	4D printing	× (Salt)	×	○	×	(Sphere)	×	×	×

Table S1. Hydrogel actuators reported in previous works.

FT-IR spectra results of citric acid-coated SPIONs

In the citric acid-coated SPIONs, the peak of Fe_3O_4 is 584.3254 cm^{-1} which is related to the stretching and torsional vibration modes of magnetite. It was observed that the peak at 1695.1220 cm^{-1} corresponds to the symmetric vibration of C=O in citric acid and the peak at 1425.1370 cm^{-1} corresponding to asymmetric C-O stretching is shifted to the peak of 1558.2010 cm^{-1} and the peak at 1398.1380 cm^{-1}, respectively, owing to the interaction between the carboxyl group of citric acid and Fe_3O_4 in citric acid-coated SPIONs.[13] This means that citric acid was successfully coated on the SPIONs surface.

Rheological properties of PNIPAM ink according to PF127 concentration and PEG ink according to SPIONs concentration

The viscosity of PNIPAM ink increases as the concentration of fugitive carrier (PF127) increases, but 31.4 wt% of PF127 collapses at a high shear rate due to many bubbles in the ink (Fig. S1a). The viscosity of the PEG inks increased as the concentration of SPIONs increased, but the difference between 0 wt% and 10 wt% was neglectable (Fig. S1d). At this time, as the PF127 concentration of the PNIPAM ink increases, the storage modulus and shear strain at the flow point increase (Fig. S1b and Fig. S1c), as the SPIONs concentration of PEG ink increases, the storage modulus increases (Fig. S1e), but the shear strain at the flow point is almost similar (Fig. S1f). Therefore, both PF127 and SPIONs concentrations affect the elasticity of the hydrogel ink. The linear viscoelastic range (LVR) increased as the PF127 concentration of PNIPAM ink and the SPIONs concentration of PEG ink increased. The yield stress (the value of the shear stress at the limit of the LVR) gets higher, as the PF127 concentration increases, while SPIONs concentration affects rarely (Fig. S1b and Fig. S1e).

Die-swelling and traction effect of hydrogel inks

Fig. S2 compares the extruded ink diameter according to each parameter setting for appropriate 3D printer parameters setting. First, viscoelastic ink is affected by die-swelling and traction effects. The die-swelling effect is a phenomenon in which the ink expands when it is extruded into the air by shear stress, and the diameter of the path line is larger than the inner diameter of the needle. The traction effect is a phenomenon in which the diameter of the ink (d) decreases as the ink is dragged and stretched as the printing speed (V) increases.[14] In this situation, the value obtained by dividing the diameter (d) of the printed ink by the inner diameter (D) of the needle is called the die-swell ratio (α). Therefore, variables that affect printing resolution include ink viscosity, inner needle diameter, extrusion amount, printing speed, and height between the needle outlet and the bottom surface (H). For all experiments, H was fixed at 0.2 mm (Fig. S2a). In addition, Fig. S2b and Fig. S2c confirmed that the die-swell ratio increases as the viscosity decreases, the inner needle diameter decreases, and the extrusion amount increases.

In Fig. S2d, when PEG ink is printed at 80%, 180%, and 280% of the extrusion amount using a 25-needle gauge, the larger the extrusion amount, the larger the extruded ink diameter and die-swell ratio. The reason for this phenomenon is that the higher the extrusion amount, the faster the extruded ink speed, and the greater the extrusion deformation, causing the recovery swelling of the ink around the needle outlet.[15] Accordingly, we finally selected 180% as the extrusion amount, not 280%, which affects by a too-large die-swelling effect, or 80%, which frequently causes cut-off while printing. Previously, since the yield stress of the ink used for multi-material printing was almost the same, PNIPAM with 24.7 wt% PF127 and PEG with 5 wt% SPIONs ink were also fixed with an extrusion amount of 180%.

Fig. S2e analyzed the die-swelling and traction effect based on variations in inner needle diameter while printing PEG ink with the extrusion amount fixed at 180%. First, when ink is extruded, a large shear force is applied to the needle outlet side due to the frictional force on the wall of the needle, resulting in a large velocity gradient in the vertical direction, resulting in a large change in shear rate. Since all of our hydrogel inks show shear thinning behavior, the high shear rate generated at the needle outlet reduces the viscosity of the ink, making it easier to extrude the ink from the needle. In this situation, the reason why the shear rate decreases as the inner needle diameter increases is expected to be due to the pressure difference around the needle outlet. The larger the inner needle diameter, the larger the flow rate, which makes it easier to extrude the ink, reducing the pressure around the needle.[16,17] Thus, as the inner needle diameter increases, the die-swell ratio decreases because the shear rate and needle outlet pressure decrease. The die-swell ratio decreases as the needle diameter increases; however, 25 gauge was selected as the output of PNIPAM and PEG ink for high-resolution printing because the extruded ink diameter was smaller for 25 gauge than 23 gauge.

Fig. S2f showed the die-swelling and traction effects of PNIPAM inks with different PF127 concentrations in a 25 gauge needle and 180% extrusion amount. In Fig. S1a, it was observed that the higher the PF127 concentration, the higher the viscosity of the ink. Since the die-swell ratio decreases as the viscosity of the ink increases, the influence of the die-swelling effect is low. This is because the higher viscosity of ink requires the higher yield stress to extrude.[18]

Printability of hydrogel inks

Fig. S4a was used to analyze printability according to PEG ink with different concentrations of SPIONs and various sizes of needle gauge at 180% of the extrusion amount. PEG inks with SPIONs 1 wt%, 5 wt%, and 10 wt% could be printed at 25, 23, and 19 gauges, respectively. The probability of SPIONs agglomerating and obstructing the needle is believed to rise with an increase in the concentration of SPIONs in the ink. Therefore, PNIPAM inks and PEG inks without SPIONs were previously selected as 25 gauge, and PEG ink with SPIONs 5 wt% was selected as 23 gauge, which is the smallest inner needle diameter that can be printed.

In Fig. S4b, printability was tested according to PF127 concentration and printing speed using an extrusion amount of 180% and a 25 gauge needle. The ink was cut off when the printing speed was 3 mm/s, regardless of the PF127

concentration. This suggests that the difference in viscosity according to the concentration of PF127 is not large enough to affect printability. However, when using PF127 16.4 wt%, it was printed larger than the design model during 3D printing due to the die-swelling effect. The image of the lid confirmed that 2 out of 4 legs of the slot were not printed (Fig S3).

Finally, the printability of PNIPAM and PEG inks was tested according to the printing speed and extrusion amount in a 25 gauge needle to determine the printing speed. When using a printing speed of 18 mm/s, it was too fast to stick ink to the bottom layer, so printing was impossible. When using an extrusion amount of 80%, 180%, and 280%, the printing line was cut off while printing at 3 mm/s, 6 mm/s, and 12 mm/s, respectively. When using an extrusion amount of 180% and a printing speed of 3 mm/s in a 25 gauge needle, the die-swell ratio is about 1.22 at PNIPAM and 1.25 at PEG ink, which is not much different from the inner needle diameter. However, when printed at 0.1 mm/s, it had a die-swell ratio of 2.59 at PNIPAM ink and 2.6 at PEG ink. As the printing speed decreases, the ink is greatly affected by die-swelling and the printing resolution decreases. Therefore, the final printing speed was selected as 3 mm/s (Fig. S4c).

Printing quality according to printing path

Based on the setting of printing parameters, the printing quality was compared according to the printing path. The image immediately after UV curing is shown in Fig. S5a, and the difference in swelling/shrinking according to temperature was confirmed in Fig. S5b to analyze the printing quality of the slot more precisely. As a result, slots were not printed at all for concentric and grid paths, and slots were printed for lines, but the ink was printed in the middle of each leg so that the slot did not open at high temperatures. Therefore, printing was carried out by selecting a custom line with a slightly modified printing path in the lines, and the slot in the form of 4 legs can be clearly printed. In addition, considering all these results, the printing parameter was finally selected as shown in Fig. S6.

References

1   V. Holzapfel, M. Lorenz, C. K. Weiss, H. Schrezenmeier, K. Landfester and V. Mailänder, *J Phys Condens Matter.,* 2006, **18**, S2581-S2594

2   D. Singh, R. K. Gautam, R. Kumar, B. K. Shukla, V. Shankar and V. Krishna, *J Water Process Eng.,* 2014, **4**, 233-241.

3   H. Arslan, A. Nojoomi, J. Jeon and K. Yum, *Advanced Science*, 2019, **6**, 1800703.3

4   H. Yuk, S. Lin, C. Ma, M. Takaffoli, N. X. Fang and X. Zhao, *Nature Communications*, 2017, **8**, 14230.

5   Y. Yao, C. Yin, S. Hong, H. Chen, Q. Shi, J. Wang, X. Lu and N. Zhou, *Chemistry of Materials*, 2020, **32**, 8868-8876.

6   X. Hu, Z. Ge, X. Wang, N. Jiao, S. Tung and L. Liu, *Composites Part B: Engineering*, 2022, **228**, 109451.

7   S. Fusco, M. S. Sakar, S. Kennedy, C. Peters, R. Bottani, F. Starsich, A. Mao, G. A. Sotiriou, S. Pané, S. E. Pratsinis, D. Mooney and B. J. Nelson, *Advanced Materials*, 2014, **26**, 952-957.

8   S. Jang and S. Park, *Sensors and Actuators B: Chemical*, 2023, **384**, 133654.

9   J. Simińska-Stanny, M. Nizioł, P. Szymczyk-Ziółkowska, M. Brożyna, A. Junka, A. Shavandi and D. Podstawczyk, *Additive Manufacturing*, 2022, **49**, 102506.

10   Y. Sun, L. Chen, Y. Jiang, X. Zhang, X. Yao and S. Soh, *Materials Horizons*, 2019, **6**, 160-168.

11   H. Son, E. Byun, Y. J. Yoon, J. Nam, S. H. Song and C. Yoon, ACS Macro Letters, 2020, **9**, 1766-1772.

12   S. Y. Zheng, Y. Shen, F. Zhu, J. Yin, J. Qian, J. Fu, Z. L. Wu and Q. Zheng, Advanced Functional Materials, 2018, **28**, 1803366.

13   H. Kim, E. Kim, S. W. Jeong, T. Ha, S, Park, S, G. Lee, S. J. Lee and S. W. Lee, *Nanoscale* 2015, **7**, 16470-16480

14   L. Zhou, H. Ramezani, M. Sun, M. Xie, J. Nie, S. Lv, J. Cai, J. Fu and Y. He, *Biomaterials Science*, 2020, **8**, 5020-5028.

15   L. Y. Zhou, Q. Gao, J. Z. Fu, Q. Y. Chen, J. P. Zhu, Y. Sun and Y. He, *ACS applied materials & interfaces*, 2019, **11**, 23573-23583.

16   F. Yang, C. Guo, M. Zhang, B. Bhandari and Y. Liu, *LWT*, 2019, **102**, 89-99.

17   T. M. Oyinloye and W. B. Yoon, *Innovative Food Science & Emerging Technologies*, 2022, **78**, 103008.

18   Q. Gao, X. Niu, L. Shao, L. Zhou, Z. Lin, A. Sun, J. Fu, Z. Chen, J. Hu and Y. Liu, *Biofabrication*, 2019, **11**, 035006.

Video S1. 3D printing process of the smart soft carrier.

Video S2. Magnetic manipulation of the smart soft carrier.

Video S3. Feasibility test of cargo delivery.

Video S4. Various and multiple cargo delivery tests.

Video S5. Magnetic manipulation and robustness test of the smart soft carrier.

Video S6. The maximum number and mass of cargoes that the smart soft carrier can handle.

Video S7. Handling of living marine organisms.

Video S8. Robustness test of the smart soft carrier with living marine organisms.